ISSN: 2688-8645

Research on the Power Matching Method of Dual-motor Driven Centrifuge

Yongwen Chen [1], Yongjun Hou [1], Changqing Mou [2], Zhe Lian [2], Yongheng Ma [2]

[1] School of Mechanical Engineering, Southwest Petroleum University, Chengdu, Sichuan, 610500, China

[2] Hebei Drilling Equipment Manufacturing Branch of Baoji Oilfield Machinery, Cangzhou, Hebei, 061000, China

Abstract

To address the power loss and high-frequency "material jamming" issues caused by improper motor selection in dual-motor driven horizontal screw discharge centrifuges, this paper proposes a motor power calculation method based on a 2K-H differential transmission mechanism to optimize motor configuration. First, the rotational speed relationships between the components of the differential are systematically analyzed using the transmission ratio method, and the external torque distribution of each component is derived using the torque balance equation, laying a theoretical foundation for power distribution. Second, taking the LW450 centrifuge as the research object, the power variation laws of the main and auxiliary motors under different drum speeds and differential conditions are explored in depth. The changing trends of the torque of the main shaft and differential input shaft with the drum speed are revealed, and the calculation results are matched with the actual pushing torque requirements to determine the optimized power configuration scheme for the main and auxiliary motors. Subsequently, electromechanical co-simulation is performed using Simulink-Recurdyn to reproduce the differential collapse phenomenon caused by insufficient braking capacity of the auxiliary motor, and it is verified that the slag production can be increased by approximately 1.8 times. Finally, a finite element analysis was conducted to investigate the impact of optimization on the centrifuge structure. The results showed that the optimized auxiliary motor's power torque can maintain balance with the frictional torque under high load, thereby reducing stress by approximately 89%. This dual-motor power matching method is also applicable to other centrifuge models, further improving the overall performance and operational stability of the centrifuge.

Keywords

Decanter Centrifuge; Differential Gear Train; Power Flow; Dynamic Analysis; Motor Configuration.

1. Introduction

As a key separation device, the performance of the horizontal screw centrifuge directly affects the material separation efficiency and system operation stability. Modern centrifuges generally adopt a dual-motor system driven by a variable frequency drive (VFD) to achieve independent and precise control of the rotation speed of the drum and screw conveyor. However, the reasonable matching of the power of the main and auxiliary motors has always been a core challenge in engineering design. Inappropriate configuration often leads to the system operating in the inefficient zone [1], which not only wastes energy but may also cause process problems such as "material jamming" due to insufficient torque.

ISSN: 2688-8645

Accurate mathematical modeling of the horizontal screw centrifuge is the basis for understanding and optimizing its performance. Early modeling work mainly focused on describing its macroscopic performance parameters [2] and key internal physical processes, such as establishing a special mathematical model for solid conveying power [3]. These studies laid the theoretical foundation for analyzing equipment behavior from a physical perspective.

In recent years, with the increasing demand for sustainable production, the research focus has shifted to improving and optimizing system energy efficiency. The new generation of centrifuges was designed with energy efficiency as the goal[4]. Tamborrino et al.[5] pioneered the establishment of a centrifuge energy consumption model equipped with a regenerative braking energy recovery system. Their conclusions have been further experimentally verified and quantified in different application scenarios[6]. In addition, researchers have also optimized energy saving through process-level control, such as by adjusting differential speed and weir depth[7][8], or by adopting advanced control strategies such as online parameter estimation[9] to improve operating efficiency and achieve energy saving. The latest research has taken the problem to a deeper level. The research of Leone et al.[10] revealed that the highest energy recovery rate is not equivalent to achieving the lowest energy consumption ratio. From the perspective of motor selection, the simulation work of Mammadov et al.[11] demonstrated the necessity of a moderate motor "overload configuration" for improving the overall efficiency of the system. And more refined parametric modeling research[12] has also provided new tools for predicting centrifuge performance.

Although existing research has achieved fruitful results in areas such as system-level energy consumption modeling, process optimization, and motor selection, most of them analyze the drive system as a whole in an input-output analysis. This has led to a general lack of theoretical guidance for the power configuration of dual-motor drive systems in engineering design practice, with most relying on calculation methods for single-motor modes [13] or empirical estimation. The drawbacks of this empirical selection are quite obvious: it not only makes it difficult to ensure that the centrifuge achieves optimal performance under varying operating conditions, but also often causes equipment overload shutdown and auxiliary motors being driven to generate electricity in reverse at high speeds. Although adaptive control systems [14][15] have alleviated the occurrence of faults to some extent, as a "post-event" adjustment method, they have failed to fundamentally solve the matching defects in the design stage, thus restricting the full performance of the centrifuge. Therefore, establishing a methodology that can systematically guide the power matching of the main and auxiliary motors based on the internal mechanical mechanism of the differential has become a new method to solve the "material jamming" problem of centrifuges.

To this end, this paper aims to fill this research gap and proposes a dual-motor power matching method based on the internal dynamic analysis of the 2K-H differential transmission mechanism. This study aims to provide a scientific theoretical basis and design criteria for motor selection and power configuration of dual-motor driven centrifuges, thereby optimizing system performance during the design phase and providing an effective technical path to solve the "material jamming" phenomenon, achieve energy saving and consumption reduction, and improve equipment operation stability.

2. 2K-H Differential Working Principle

As a crucial piece of equipment for solid-liquid separation in the chemical industry, the design of the transmission system in a horizontal decanter centrifuge directly impacts separation efficiency and operational stability. Traditional transmission systems employ simple open kinematic chains, failing to achieve efficient speed difference control between the drum and the propeller, leading to increased motor power demands, higher energy consumption, and a bulky

ISSN: 2688-8645

transmission structure. Modern horizontal decanter centrifuges have shifted to a design based on planetary gear differentials. This improvement not only enhances transmission efficiency but also significantly improves the equipment's compactness and reliability. Currently, centrifuges widely utilize planetary gear differentials as the core of their transmission, consisting of a sun gear, planetary gears, a ring gear, and a planet carrier. These differentials are compact, offer high transmission ratios and high efficiency, and can achieve high torque output within a limited space.

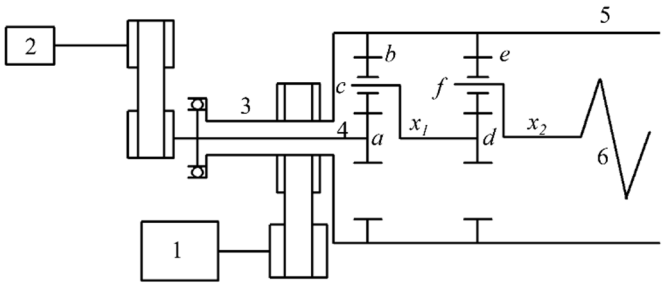

Fig 1. 2K-H dual-stage differential structure diagram

Figure 1 shows the 2K-H differential transmission system used in the dual-motor drive. The gear rings b and e are typically connected to the drum 5, while the planetary carrier x_2 is connected to the propeller 6. The main motor outputs power to the gear ring via belt drive, providing the operating speed for the drum. The auxiliary motor drives the sun gear a to rotate via a pulley, synthesizing the input speed into a new speed through the differential and transmitting it to the propeller. During centrifuge operation, adjusting the speed of the auxiliary motor allows for regulation of the speed difference between the drum and the propeller.

2.1. Calculation of Kinematic Parameters of 2K-H Differential

2.1.1. Rotational Speed Calculation

Based on the method for calculating the transmission ratio of planetary gear transmission[16], the rotational speed relationship between the sun gear, planet gears, ring gear, and planet carrier can be calculated. On this basis, by combining the rotational speed equations of the first and second stage gear transmissions, the mathematical relationship between the differential speed (speed difference between the drum and the propeller) and the rotational speed of the drum and differential input shaft shown in equation (1) can be further derived:

$$p_1 = \frac{z_b}{z_a}, p_2 = \frac{z_e}{z_d}, \Delta\omega = \omega_b - \omega_{x_2}, \quad \omega_b - \omega_a = (1+p_1)(1+p_2)\Delta\omega \tag{1}$$

Here, z_a、z_d、z_b、z_e, These are the number of teeth on the sun gear and the ring gear, respectively, and are dimensionless. ω_a、ω_b、ω_{x_2} These are the rotational speeds of the sun gear, ring gear, and planet carrier, respectively, rad/s.

2.1.2. Torque Calculation

Through force analysis of the gear train [16] and the power conservation equation of the system, the external torque relationship of the two-stage 2K-H mechanism is derived:

$$T_{x_2} = -(1+p_1)(1+p_2)T_a \tag{2}$$

Here, T_{x_2} is the frictional torque of the sediment on the propeller; T_a is the external torque acting on the sun gear a, N·m.

2.2. System Equilibrium Moment Equations

In the differential-centrifuge system, the sediment on the right end generates frictional torques of equal magnitude and opposite direction on the drum and the propeller. The frictional torque

ISSN: 2688-8645

generated by the sediment on the propeller is in the same direction as its rotation because the sediment rotates at high speed with the drum, while the propeller rotates at a slower speed and lags behind, forming a positive driving torque. When bearing friction and air resistance are ignored, according to the principle of torque balance of the system, the torque of the main shaft on the left end is equal in magnitude and opposite in direction to the torque of the differential input shaft. However, in actual operation, friction between the drum and the bearing and air resistance will cause losses, so the torque balance equation shown in formula (3) is established:

$$T_1 + T_k + T_z = -T_a \tag{3}$$

By substituting Eq. (2) into the first six equations of Eq. (3), the following result can be obtained:

$$T_1 = \frac{T_{x_2}}{(1+p_1)(1+p_2)} - T_k - T_z \tag{4}$$

Here, T_1 is the main spindle torque, N·m; T_k is the air friction torque, N·m; T_z is the bearing friction torque, N·m.

2.3. Main and Auxiliary Motor Status Analysis

First, define the input power into the system as positive and the output power as negative, that is, P=T*W>0 for input power into the system and P=T*W<0 for output power into the system. Then, according to the power definition P=T*W, the power of the main and auxiliary motors and the power loss are obtained. Expression (5):

$$P_1 = T_1\omega_b, P_2 = T_a\omega_a, N_k = T_k\omega_b, N_z = T_z\omega_b \tag{5}$$

Here, P_1 and P_2 are the power of the main and auxiliary motors, respectively; N_k is the power loss due to friction between the drum and the air, kw; N_z is the power loss due to friction between the drum and the bearing, kw.

Definition of pushing power: Pushing power refers to the power consumed by the screw propeller in overcoming the frictional torque between the material and the inner wall of the drum to push the solid material from the inside of the drum to the slag discharge port[13]. This process can be described by formula (6):

$$N_s = -T_{x_2} \times \omega \tag{6}$$

Here, N_s represents the pushing power, kw;

The propeller is driven to rotate by the planetary carrier in the secondary structure. The frictional torque on the propeller is regarded as the external torque on the planetary carrier. The relationship between the pushing power and the power of the main motor and the auxiliary motor can be obtained from formulas (4) and (6):

$$N_s = -T_{x_2} \times \omega = -(T_1 + T_k + T_z)\omega_b - T_a\omega_a \tag{7}$$

From the relationship between motor power and pushing power shown in equation (7), three states of the main and auxiliary motors can be derived.

State 1): $\omega_b > 0$, $\omega_a < 0$, that is, the two motors rotate in opposite directions, $P_1 + P_2 = -(N_s + N_k + N_z)$, at this time both the main and auxiliary motors input power into the system;

State 2): $\omega_b > 0, \omega_a > 0$, the two motors rotate in the same direction, $P_1 = -(N_s + P_2 + N_z + N_k)$, at this time the main motor inputs power into the system, and the auxiliary motor acts as a braking motor, consuming part of the energy of the main motor;

State 3): $\omega_a = 0$, at this time only the main motor drives the centrifuge system to work.

ISSN: 2688-8645

3. Centrifuge Motor Power Configuration Analysis

According to the calculation formula of friction torque[13] and formula (1)-(7), the centrifuge speed is set to four differential speed ranges according to the on-site centrifuge speed adjustment method: $n_a = 1350$ rpm, $n_b = 1600 - 4000$ rpm; $n_a = 1125$ rpm, $n_b = 1600 - 4000$ rpm; $n_a = 900$ rpm, $n_b = 1600 - 4000$ rpm; $n_a = 0$ rpm, $n_b = 1600 - 4000$ rpm. Figure 2 shows the influence of the spindle speed and the differential input shaft speed on the friction torque: when the differential input shaft speed remains unchanged, as the spindle speed increases, the speed difference between the drum and the propeller increases, and thus the friction torque also increases; while under the condition of constant spindle speed, the effect of adjusting the differential input shaft speed on the change of friction torque is limited, indicating that the drum speed plays a dominant role in the formation of friction torque.

Since the friction torque values calculated in different differential speed ranges are relatively small under the same spindle speed conditions, this study selects the friction torque variation curve at 3200 rpm as the calculation parameter to simplify subsequent analysis and ensure the consistency and accuracy of subsequent analysis.

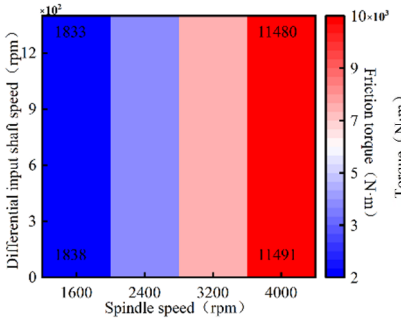

Fig 2. Friction torque variation

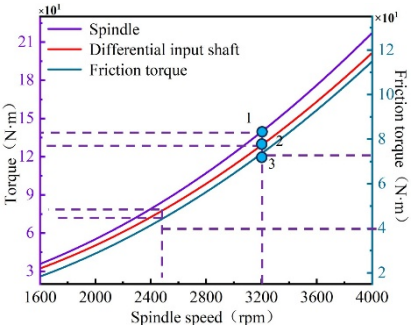

Fig 3. Friction torque and torque curve

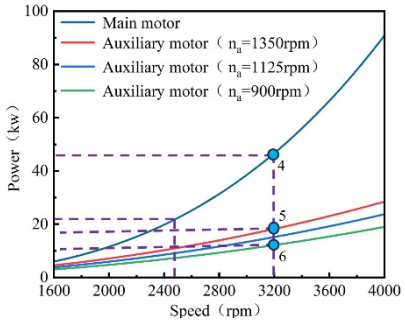

Fig 4. Power change curve

Figure 3 shows that as the drum speed increases, the main shaft torque, differential input shaft torque, and friction torque all show a significant upward trend, reaching a peak at 4000 rpm. After determining the maximum operating speed of the centrifuge, the perpendicular line drawn from the operating speed point in the figure intersects with the three curves. The intersection points (1, 2, 3) are then used to draw horizontal lines to both sides, and the intersections with the vertical axis are the corresponding torque and friction torque values. Taking a drum speed of 3200 rpm as an example, the main shaft torque is N·m, the differential input shaft torque is N·m, and the friction torque is 7346 N·m. From formula (3), it can be seen that the torques of the main shaft and the differential input shaft are in opposite directions, so only their absolute values are discussed in the following analysis.

Based on the torque variation curve shown in Figure 3, the power variation curves of the main and auxiliary motors with the drum speed in each differential speed range in Figure 4 were calculated using formula (5)-(7). The results show that the power of both the main and auxiliary motors reaches its maximum value when the drum speed reaches 4000 rpm. After determining

ISSN: 2688-8645

the operating speed and speed difference range of the centrifuge, the power configuration of the main and auxiliary motors under the corresponding operating conditions can be obtained by using the vertical-horizontal line reading method. For example, when the spindle speed is 3200 rpm and the speed difference is 29 rpm (intersection point 5), the power configurations of the main and auxiliary motors are 46.8 kW and 18.2 kW, respectively; when the speed difference increases to 37 rpm (intersection point 6), the corresponding power configurations are 46.8 kW and 12.1 kW. Figure 4 shows the power matching curves of the main and auxiliary motors of the LW450 centrifuge under any operating speed and speed difference conditions, providing an intuitive and reliable basis for motor selection and power configuration.

4. Electromechanical Joint Simulation Analysis of Drilling Fluid Centrifuge

4.1. Simulation Model

During the slag conveying process of the screw propeller, the frictional torque generated by the relative sliding of the slag with the inner wall of the drum and the blades of the screw propeller pushes the slag to the solid discharge port for unloading. Through the force analysis of the slag, it is found that its frictional torque is related to factors such as the half cone angle α of the drum and the helical angle β. Taking the LW450 centrifuge as an example, its relevant parameters are as follows:

$$M = 1500\ \text{kg},\ L = 1.35\ \text{m},\ r_1 = 225\ \text{mm}, r_2 = 80\ \text{mm},\ \alpha = 9.5°,\ \beta = 6.9°,\ f_1 = f_2 = 0.3$$

Here, M is the mass of the centrifuge, kg; L is the length of the drum, mm; r_1 is the inner diameter of the drum, mm; r_2 is the minor diameter of the helical blade, mm; α is the semi-cone angle, °; β is the helix angle, °; f_1 and f_2 are the friction coefficients of the sludge on the drum and the helical propeller, respectively, dimensionless.

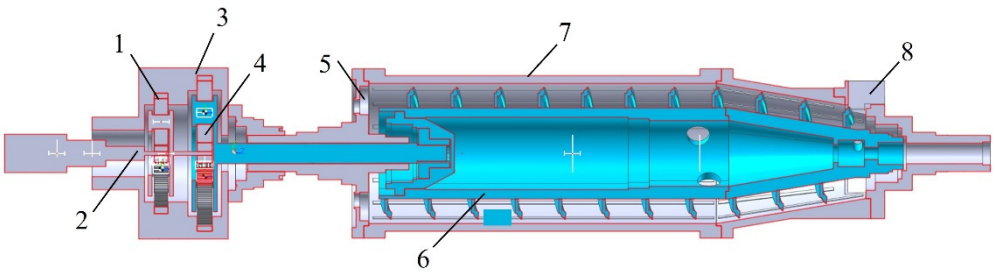

Fig 5. Differential Model

1-Ring gear 2-Sun gear 3-Differential housing 4-Planet gears 5-Overflow port 6-Screw propeller 7-Drum 8-Slag discharge port

Based on the transmission characteristics of the dual-drive centrifuge, a simplified three-dimensional model of the differential was constructed using SolidWorks software (as shown in Figure 5). By consulting planetary gear design data [16], the specific parameters of each gear were determined:

The friction torque formula[13] is used to calculate:

$$n_b = 3200\ \text{rpm},\ n_a = 918\ \text{rpm}, M_z = 6573\ \text{N·m}, T_k = 3.5\ \text{N·m}, T_z = 7\ \text{N·m}$$

$$m_1 = 6, z_a = 13, z_b = 77, z_c = 32;\ m_2 = 4, z_d = 13,\ z_e = 89, z_f = 38$$

4.2. Simulation Reproduction of the "Material Jamming" Failure Mechanism in Traditional Configuration Schemes

To investigate the underlying mechanism by which the traditional motor configuration (37kW main motor and 7.5kW auxiliary motor) causes a decrease in the centrifuge's slag removal

ISSN: 2688-8645

capacity or even "material jamming" failure when handling challenging conditions such as drilling fluids with high solids content, this study dynamically reproduced and analyzed the failure process based on the established RecurDyn-Simulink electromechanical coupling co-simulation model.

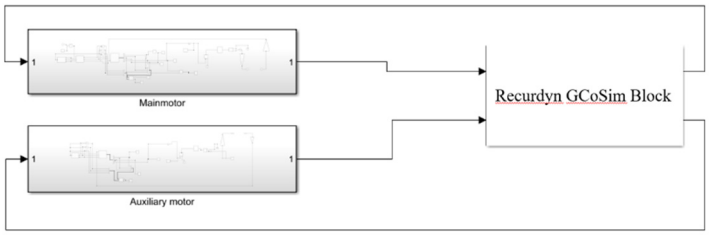

Fig 6. Co-simulation diagram

4.2.1. Simulation Conditions and Loading Strategies

In the initial stage of the simulation, the system operated under no-load. The auxiliary motor started and reached a stable speed within 0-15 seconds, while the main motor started at 15 seconds. By 160 seconds, the entire system had entered a stable no-load operating state. To simulate the enormous pushing resistance experienced by the screw conveyor when a centrifuge processes high-concentration materials, this study employed a step function to apply equal and opposite frictional torques between the screw propeller and the drum. The specific loading strategy is as follows:

1) First-stage loading (simulating high-load conditions): At 160s, a frictional torque of 7346 N·m is applied (step(time, 160, 0, 163, 7346000), with a 3s ramp-up time set for easier observation of dynamic response). This value simulates the ultimate pushing resistance of the screw conveyor at a drum speed of 3200rpm.

2) Second-stage loading (simulating overload conditions): At 170s, the frictional torque is further increased to 8346 N·m (step(time, 170, 0, 173, 1000000)) to observe the dynamic behavior of the system after exceeding the design limits.

4.2.2. Simulation Results and Failure Mechanism Analysis

Through comprehensive analysis of the simulation results, the dynamic evolution process of "material jamming" failure can be clearly revealed, as shown in Fig.7-Fig.10.

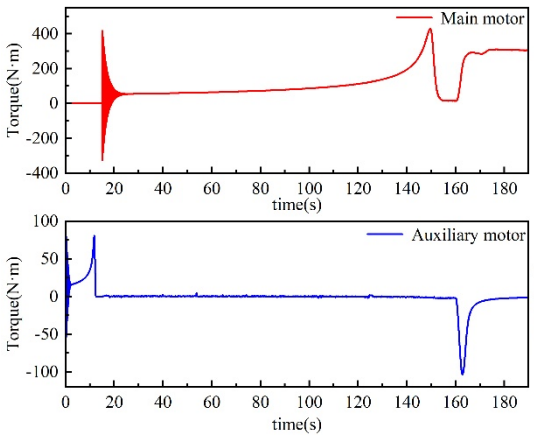

Fig 7. Output torque curve

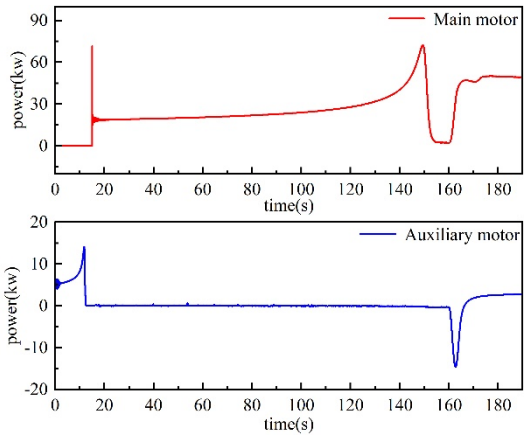

Fig 8. Power consumption curve

After a load is applied for 160 seconds, the main motor (red line) rapidly increases its output torque and power to nearly 300 N·m and approximately 47 kW respectively to counteract the braking torque at the drum end. It then maintains a relatively stable drum speed for a short period due to its overload capacity. Simultaneously, the auxiliary motor (blue line) switches from drive to regenerative braking, with both its output torque and power becoming negative.

ISSN: 2688-8645

Simulations show that the 7.5 kW auxiliary motor's maximum braking torque is insufficient at this point, and the braking torque transmitted to the screw end is less than the material driving torque, causing its braking capacity to reach its limit and becoming the main bottleneck in the system's processing capacity under high load conditions.

The speed curve (Figure 9) visually reveals the system failure process: when the auxiliary motor's braking capacity reaches saturation, it can no longer effectively constrain the screw conveyor's speed. The speeds of the differential input shaft (blue line) and the screw conveyor (pink line) then rapidly increase and approach the drum (red line), causing the differential speed between the drum and the screw to rapidly decrease and approach zero. Since the differential speed is a key parameter for solid-phase axial conveying, its collapse means that the screw's scraping and pushing function relative to the drum fails, the material cannot be continuously discharged and accumulates in the separation zone, ultimately causing a "material jam" fault.

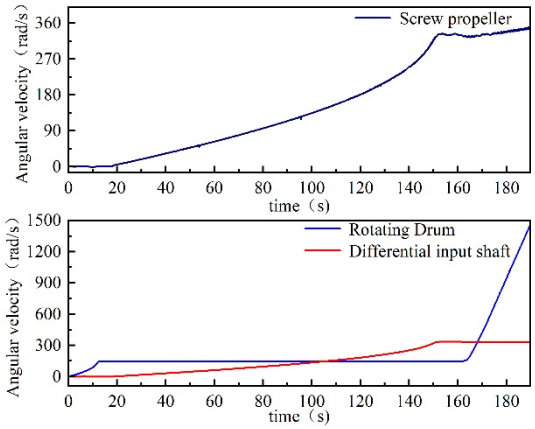

Fig 9. Rotational speed curve

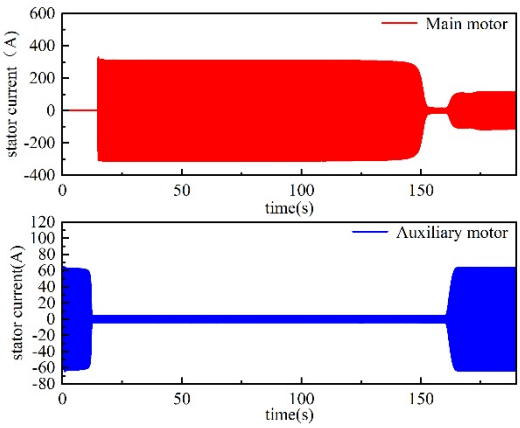

Fig 10. Stator current curve

The stator current curve (Figure 10) confirms the system's dynamic response from an electrical perspective. During the startup phase (15–155 s), the main motor draws a peak starting current of nearly 300 A to overcome the large inertia of the drum. After reaching its rated speed at approximately 155 s, the current gradually decreases, consistent with the startup characteristics of a high-inertia load. After steady-state operation (after 155 s), the current mainly varies with the load: when a high load impact is applied at 160 s, the auxiliary motor's stator current surges to more than 7 times its rated value due to its braking capacity approaching its limit, indicating that the system is in a near-instability state.

Simulation results show that the key bottleneck of the system lies in the braking capacity of the auxiliary motor: under high load impact, the material driving torque on the screw conveyor exceeds the maximum braking torque of the auxiliary motor, causing the auxiliary motor to stall and lose its constraint on the screw speed. The differential speed rapidly decays to zero, the slag discharge function fails, and ultimately "material jamming" occurs. Therefore, the fundamental defect of the traditional solution is that the braking torque level of the auxiliary motor is too low and does not match the actual load requirements, thus limiting the system's processing capacity and operational stability.

4.3. Performance Verification and Comparative Analysis of Optimized Configuration Schemes

Based on the insightful analysis of the performance bottlenecks of the traditional configuration scheme in Fig.4, this study employs the proposed power matching method to determine the optimized drive scheme as follows: a main motor of 55kW and an auxiliary motor of 22kW. To quantitatively verify the effectiveness of this optimized scheme and to visually compare its

ISSN: 2688-8645

performance differences with the traditional scheme, this section uses the exact same simulation conditions and loading strategies as in Section 4.2 to conduct a simulation analysis of the dynamic response of the optimized scheme.

4.3.1. Simulation results of Dynamic Response of the Optimization Scheme

The load application method is consistent with the traditional scheme. After applying an extreme load (7346 N·m) for 160 s in simulation time, the torque and power of the main motor (red) rapidly increased and stabilized at approximately 300 N·m and 47 kW, respectively, still within the allowable overload range and able to continuously provide stable driving force. Simultaneously, the auxiliary motor (blue) entered regenerative braking mode, with the braking torque stabilizing at approximately -123 N·m, corresponding to a braking power of approximately -18.5 kW. The results show that, under optimized configuration, the auxiliary motor can continuously output sufficient braking torque within its capacity, effectively offsetting the material driving torque on the screw conveyor. Compared to the traditional scheme where the auxiliary motor quickly reaches its limit and fails under impact load, the optimized scheme has a more sufficient braking margin and a more reasonable power-torque match.

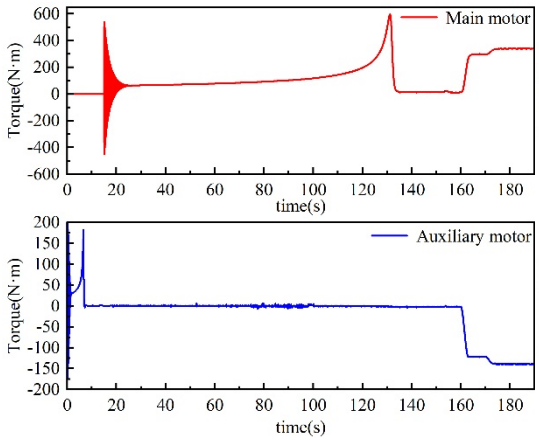

Fig 11. Output torque curve

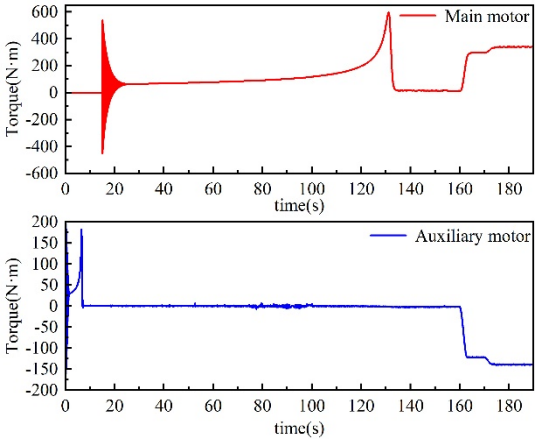

Fig 12. Power consumption curve

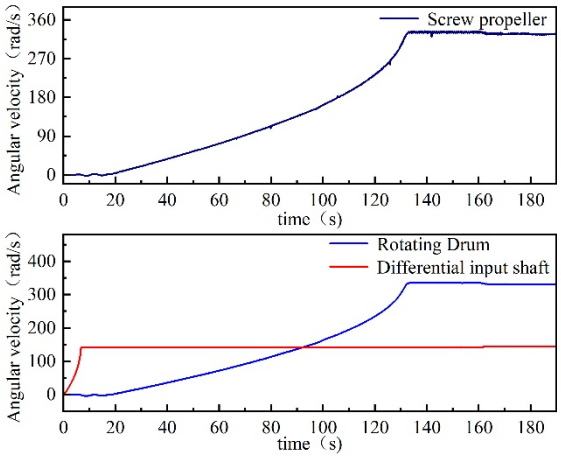

Fig 13. Rotational speed curve

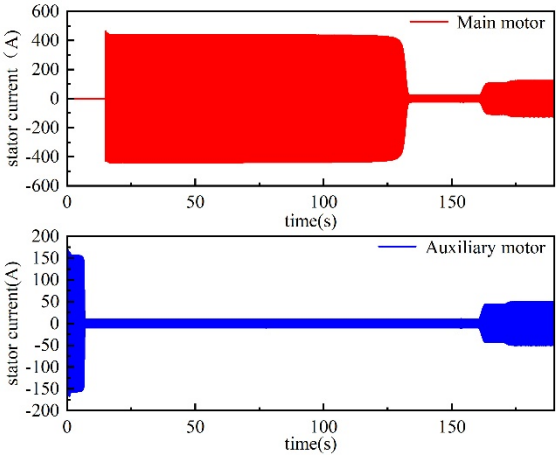

Fig 14. Stator current curve

The speed response curves in Figure 13 visually verify the effectiveness of the optimized scheme. Simulation results show that the drum (red) and screw conveyor (blue) maintain a stable differential speed throughout the startup and loading process; especially after applying an extreme load impact at 160 s, the screw conveyor speed did not experience the runaway increase seen in the traditional scheme, but was constrained by the auxiliary motor to near the target speed, only producing transient fluctuations with small amplitudes. The continuous

ISSN: 2688-8645

stability of the differential speed ensures the normal operation of the screw conveyor's pushing and slag-discharging function relative to the drum, thereby realizing the continuous conveying and discharge of solid materials and avoiding "material jamming" failure caused by differential speed collapse.

The stator current response further verified the system's operating status. During the simulation, the main and auxiliary motor currents remained stable and continuous with load changes. Especially in the high-load stage after 160 seconds, although the auxiliary motor current increased, the waveform remained smooth and stable, without the violent oscillations caused by near instability in the traditional scheme.

To verify the effectiveness of the power matching method proposed in this study, a quantitative comparison was conducted between the traditional and optimized configuration schemes in terms of their upper processing capacity limits. By applying the same, step-increasing equivalent feed load to the simulation models of the two configurations, their respective performance "inflection points" can be accurately captured. The simulation comparison results are shown in Fig. 15 and Fig. 16.

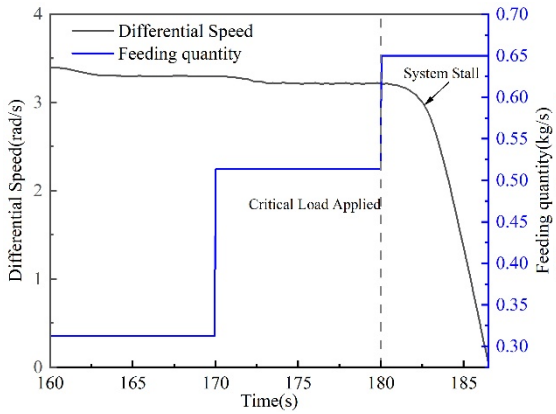

Fig 15. Traditional motor processing capacity

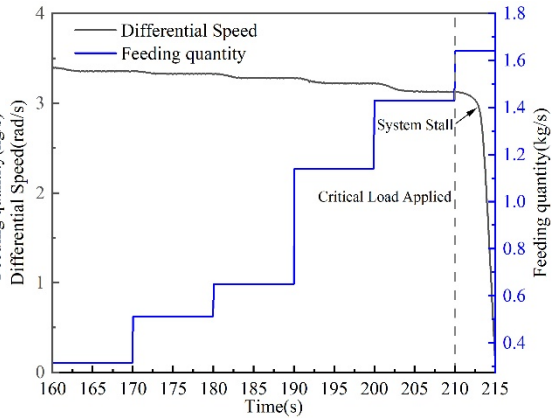

Fig 16. optimized motor processing capacity

By employing the power matching method proposed in this study, the drive scheme was optimized from the traditional 37kW-7.5kW to 55kW-22kW, increasing the centrifuge's maximum stable processing capacity from approximately 0.5 kg/s to 1.4 kg/s, a performance improvement of up to 180%. This stark and quantitative comparison irrefutably demonstrates that the performance bottleneck caused by the "capacity mismatch" of the auxiliary motor in the traditional scheme is real and severely restricts the equipment's potential. The optimized matching method based on dynamic torque demand proposed in this study effectively solves this bottleneck, fundamentally ensuring the centrifuge's operational reliability under high-load conditions and significantly improving its core process performance indicator—processing capacity. This conclusion provides the most direct and solid evidence supporting the correctness and practical value of this research.

5. Analysis of the Impact of Power Matching Scheme on Propeller Structure

The preceding chapters have demonstrated, from an electromechanical system perspective, the functional risk of "material jamming" failure due to insufficient braking capacity of the auxiliary motor in traditional configuration schemes. However, "material jamming" is not only a functional failure; the dynamic impact generated at the moment of failure can also pose a serious threat to the structural integrity of the equipment's core components. To quantitatively assess the potential destructiveness of "material jamming" from a structural mechanics perspective and further verify the value of the optimized scheme in improving equipment safety and reliability, this study uses the finite element analysis software Ansys Mechanical to

ISSN: 2688-8645

conduct a comparative analysis of the propeller structural response under two key operating conditions.

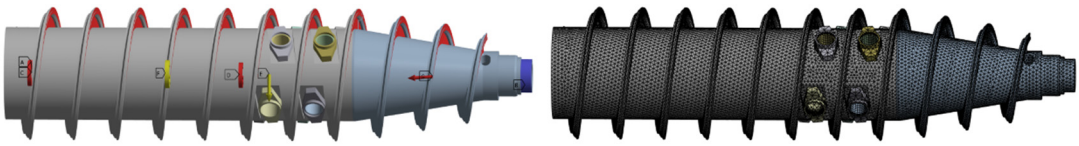

Fig 17. Load addition and mesh generation

To compare the structural responses of the optimized and traditional schemes under ultimate loads, this paper sets two typical operating conditions:

Condition A: Steady-state ultimate load. This simulates the stable operating state of the optimized configuration under ultimate pushing torque, maintaining torque balance. In the simulation, an equivalent static load torque of 7346 N·m is applied to the propeller, constraining it to maintain stable differential motion to evaluate the quasi-static structural response under controllable high load.

Condition B: Dynamic stall impact. This simulates the torque imbalance and stall impact process caused by insufficient braking capacity in the traditional configuration. In the simulation, an external friction torque of 7346 N·m is applied, while only an insufficiently balanced internal braking torque of 3064 N·m is provided to equivalently represent the dynamic impact load at the moment of stall and evaluate its structural risk.

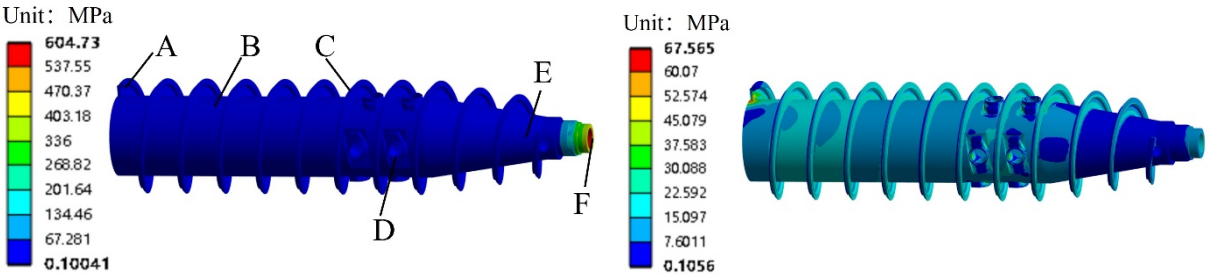

(a) Traditional configuration scheme (b) Optimized configuration scheme

Fig 18. Overall stress contour diagram

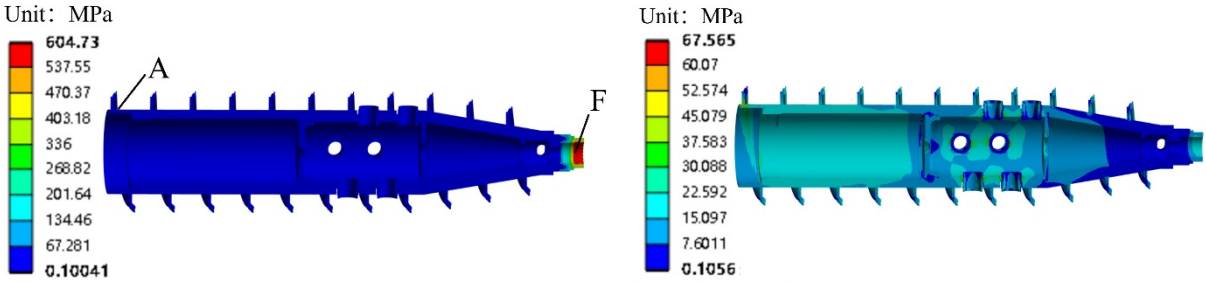

(a) Traditional configuration scheme (b) Optimized configuration scheme

Fig 19. Cross-sectional stress contour diagram

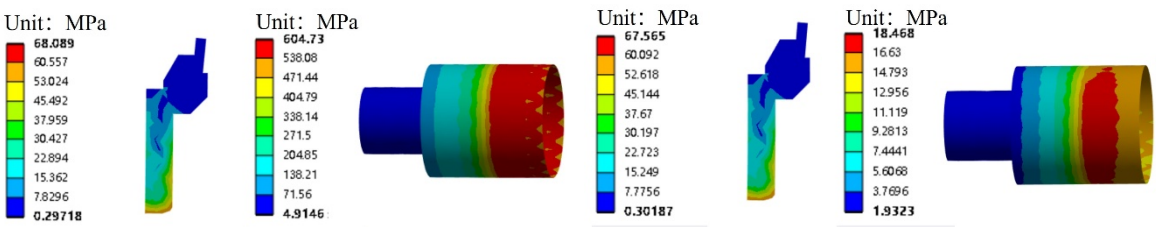

(a) Traditional configuration scheme (b) Optimized configuration scheme

Fig 20. stress contour diagram at points A and F

ISSN: 2688-8645

As can be seen from the overall and cross-sectional equivalent stress cloud diagrams, the critical area of the propeller under extreme conditions is mainly concentrated in the end connection/transition region (most typically near point F). In the traditional configuration, significant stress concentration occurs at this location, forming a global peak (maximum equivalent stress reaching 604.73 MPa). This indicates that the braking torque provided by the auxiliary motor cannot balance the frictional torque, causing the load to increase during transmission, and structural safety is dominated by the peak stress at the end.

After improving the braking torque capability of the auxiliary motor, the stress field distribution becomes more uniform, the high-stress zone at the end shrinks significantly, and the overall peak stress drops to 67.565 MPa. Furthermore, the local stress at point F decreases from 604.73 MPa to 18.468 MPa, while the stress at point A remains essentially at the same order of magnitude (approximately 68 MPa). This demonstrates that the key role of improving braking capability is to suppress the transient impact and bending-torsional coupling amplification effect caused by sudden changes in differential speed/torque, achieving load "peak reduction," thereby significantly reducing end stress concentration and improving the structural load-bearing safety margin.

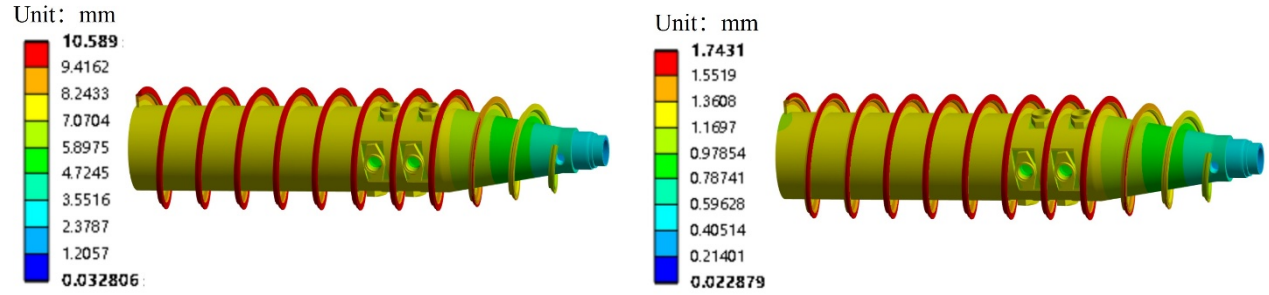

(a) Traditional configuration scheme (b) Optimized configuration scheme

Fig 21. Overall deformation

As can be seen from the overall deformation cloud map, there are also significant differences in the amplitude of the structural deformation response under extreme conditions: the maximum deformation of the traditional configuration reaches 10.589 mm, which is an amplified feature of the superposition of overall deflection and local deformation. Large deformation may cause changes in assembly clearance, deterioration of contact state and increase of secondary load, which in turn exacerbates stress concentration. After the braking capacity is improved, the maximum deformation drops to 1.7431 mm, the deformation distribution is more gradual and the overall stiffness is more stable. This indicates that the dynamic response of the system under high load disturbance is effectively suppressed, the structural geometric stability and operating clearance are easier to maintain, thereby reducing the risk of additional loads induced by large deformation and improving he reliability under extreme conditions.

6. Conclusion

This study addresses the mismatch between motor power and process load in dual-motor-driven decanter centrifuges caused by traditional experience-based sizing, which can lead to material jamming (“blocking”) failures and increased energy consumption. A theoretical analytical model and a high-fidelity electromechanical co-simulation platform were developed to systematically investigate the power-flow characteristics and dynamic responses. The main conclusions are as follows:

(1) Based on torque equilibrium, a mathematical relationship among the main shaft torque, the differential gearbox input-shaft torque, and the sludge friction torque was established. Under typical solids-discharge conditions, the auxiliary motor is not a power input unit; instead, it

operates continuously in regenerative braking mode, providing a precisely controlled braking torque to maintain the differential speed while absorbing part of the excess power delivered by the main motor.

(2) To overcome the limitations of conventional sizing methods, a new dual-motor power-matching approach based on the internal power-flow characteristics of the differential transmission was proposed. Combined with co-simulation, the method accurately reproduced the "blocking" failure process of the conventional configuration and quantitatively identified its performance bottleneck—insufficient braking capability of the auxiliary motor. Based on this diagnosis, an optimized design was obtained to ensure that the new configuration satisfies the torque demand under extreme operating conditions.

(3) The effectiveness of the optimized configuration was verified and the performance improvement was quantified. Taking an LW450 centrifuge as an example, upgrading the drive configuration from 37 kW/7.5 kW to 55 kW/22 kW increased the maximum stable throughput from 0.5 kg/s to 1.4 kg/s. The optimized scheme eliminates the risk of "blocking" at the root and significantly enhances operational stability and reliability under high-load conditions, demonstrating the correctness and strong engineering value of the proposed matching method.

(4) Finite-element structural analysis further revealed the potential structural damage induced by "blocking" failures. The results show that, under the conventional configuration, the dynamic stall impact during a "blocking" event can raise the peak stress in the screw conveyor to 604.73 MPa, exceeding the material yield limit and posing a high risk of permanent structural damage. In contrast, by maintaining dynamic balance, the optimized configuration limits the steady-state stress under extreme conditions to a safe level of 67.5 MPa. This comparison ultimately confirms, from a structural mechanics perspective, the decisive importance of scientifically grounded power matching for safe and reliable operation.

References

[1] Latchoomun L, Gokhool C, Ah King R T F, et al. Efficiency of VFD Coupled Induction Motors Operating in the Scalar Mode with Different Types of Loads[C]//International Conference on Emerging Trends in Electrical, Electronic and Communications Engineering. Cham: Springer International Publishing, 2018: 45-59.

[2] Leone A, Romaniello R, Zagaria R, et al. Mathematical modelling of the performance parameters of a new decanter centrifuge generation[J]. Journal of Food Engineering, 2015, 166: 10-20.

[3] Bell G R A, Symons D D, Pearse J R. Mathematical model for solids transport power in a decanter centrifuge[J]. Chemical Engineering Science, 2014, 107: 114-122.

[4] Hermeler J, Horstkötter L, Hartmann T. New decanter generation with improved energy efficiency [J]. FS Filtr. Sep, 2013, 13: 30-37.

[5] Tamborrino A, Perone C, Catalano F, et al. Modelling energy consumption and energy-saving in high-quality olive oil decanter centrifuge: Numerical study and experimental validation[J]. Energies, 2019, 12(13): 2592.

[6] Perone C, Berardi A, Dellisanti C D, et al. Investigation of an Energy-Saving System to Reduce the Energy Consumption of Decanter Machine[J]. Chemical Engineering Transactions, 2023, 102: 157-162.

[7] Tamborrino A, Squeo G, Leone A, et al. Industrial trials on coadjuvants in olive oil extraction process: Effect on rheological properties, energy consumption, oil yield and olive oil characteristics[J]. Journal of Food Engineering, 2017, 205: 34-46.

[8] Caponio F, Squeo G, Brunetti L, et al. Influence of the feed pipe position of an industrial scale two-phase decanter on extraction efficiency and chemical-sensory characteristics of virgin olive oil[J]. Journal of the Science of Food and Agriculture, 2018, 98(11): 4279-4286.

ISSN: 2688-8645

[9] Larsen J A, Alstrøm P. Online Paramter Estimation for a Centrifugal Decanter System[J]. IFAC Proceedings Volumes, 2014, 47(3): 9359-9363.

[10] Leone A, Perone C, Berardi A, et al. Energy analysis and numerical evaluation of the decanter centrifuge for wastewater management to allow a sustainable energy planning of the process[J]. Energy Conversion and Management: X, 2024, 22: 100596.

[11] Mammadov O, Altieri G, Genovese F, et al. Simulation of Different Control Strategies of a Three-Phase Induction Motor Coupled to a Real Decanter Centrifuge for Olive Oil Extraction Focusing on Energy Saving[J]. Applied Sciences, 2024, 14(15): 6624.

[12] Bai C, Park H, Wang L. A Model–Based Parametric Study of Centrifugal Dewatering of Mineral Slurries[J]. Minerals, 2022, 12(10): 1288.

[13] Sun, Q., Jin, D. Principles, Structure, and Design Calculations of Centrifuges [M]. Beijing: China Machine Press, 1987.

[14] Wang, B., Zhang, Z., Zhao M. et al. Development of an intelligent control system for a high-speed drilling-fluid centrifuge[J]. Mechanical Engineer, 2018, (11): 99–101.

[15] Ding, J., Wang, F., Liu, G. et al. Design of an intelligent control system for a novel horizontal decanter centrifuge[J]. Automation & Instrumentation, 2018, 39(7): 20–23.

[16] Rao, Z. Design of Planetary Gear Transmissions [M]. Beijing: Chemical Industry Press, 2003: 43–45.